ACS APPLIED MATERIALS & INTERFACES

Research Article

Cite This: ACS Appl. Mater. Interfaces 2019, 11, 30437−30445

www.acsami.org

Atomic Layer Deposition of Transparent p-Type Semiconducting Nickel Oxide Using Ni($^{t\mathrm{Bu2}}$DAD)$_2$ and Ozone

Konner E. K. Holden,[†] Charles L. Dezelah,[‡,§] and John F. Conley, Jr.*[,†]

[†]School of Electrical Engineering and Computer Science, Oregon State University, Corvallis, Oregon 97331, United States

[‡]EMD Performance Materials, Haverhill, Massachusetts 01832, United States

Supporting Information

ABSTRACT: A novel atomic layer deposition (ALD) process for nickel oxide (NiO) is developed using a recently reported diazadienyl complex, Ni($^{t\mathrm{Bu2}}$DAD)$_2$, and ozone. A window of constant growth per cycle is found between 185 and 200 °C at 0.12 nm/cycle, among the highest reported for ALD NiO. For films deposited at 200 °C, grazing-incidence X-ray diffraction indicates a randomly oriented polycrystalline cubic NiO phase. X-ray photoelectron spectroscopy shows good agreement with bulk NiO reference spectra and no detectable impurities. Atomic force microscopy reveals low root mean square roughness of 0.6 nm for an 18 nm thick film. The refractive index of 2.36 and an electronic bandgap of 3.78 eV, as determined by variable angle spectroscopic ellipsometry, are close to reported values for bulk and thin film NiO. Finally, fabricated Ag/NiO/n-Si/In heterojunction diodes show a current−voltage asymmetry of 1.27 × 10^4 at 2.3 V and an ideality factor of 3.5, confirming the intrinsic p-type semiconducting behavior of transparent NiO.

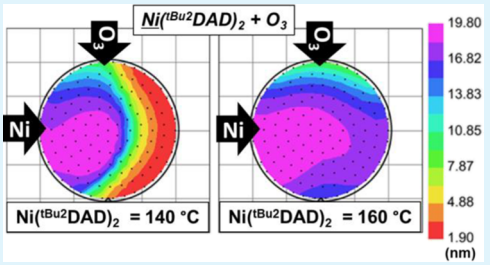

KEYWORDS: *atomic layer deposition, ALD, nickel oxide, NiO, transparent oxide semiconductors, transition metal oxides, p-type*

INTRODUCTION

Transparent wide bandgap n-type semiconducting transition metal oxides (TMOs), such as ZnO, In_2O_3, SnO_2, Ga_2O_3, InGaZnO, ZnSnO, TiO_2, etc. are fairly common and have found widespread use in a variety of applications. On the other hand, p-type TMOs are highly desired, but relatively less common and less understood.[1] Among p-type TMOs such as SnO, NiO, Cu_2O, and Co_3O_4, nickel(II) oxide (NiO) has recently garnered attention for potential application in electrical and optical devices. NiO adopts the rock salt (cubic) structure and its wide direct bandgap of 3.4−3.8 eV gives rise to optical transparency. The intrinsic p-type nature of NiO is attributed to nonideal stoichiometry created by the presence of a stable Ni^{3+} oxidation state (Ni_2O_3), giving rise to naturally occurring Ni vacancies that act as acceptor sites. NiO has seen recent application in thin-film transparent heterojunction pn diodes,[2−7] and its relatively low electron affinity of 1.8 eV also makes it a promising candidate as an electron-blocking/hole-transporting layer for solar cells.[8−11] Additionally, metal/insulator/metal tunnel diodes based on NiO have been investigated for THz frequency mixing/detection and energy harvesting due to the nonlinear and asymmetric current−voltage characteristics and ultrafast electron transit times arising from quantum tunneling through NiO.[12−17] Finally, NiO is also reported as having the ability to change resistance states in resistive random-access memory devices.[18,19]

Although, thin film NiO has been deposited using a variety of different techniques, such as spray pyrolysis,[20,21] chemical vapor deposition,[22] physical vapor deposition,[2−4,23] and pulsed laser deposition,[5−7,11] the material properties of these films typically suffer due to chemical impurities, structural nonuniformity, and relatively poor control over film thickness on the nanometer scale. These undesired properties can negatively impact optical and electronic properties. Atomic layer deposition (ALD) is based on sequential, purge-separated, self-limiting surface reactions of precursors and coreactants which enables atomically precise layer-by-layer growth that is, by nature, highly uniform and highly conformal. ALD is ideally suited for the deposition of high quality, pinhole-free, conformal films. Robust ALD processes for TCOs is of increasing interest, particularly for the aforementioned applications, and a number of ALD processes for NiO have recently been reported, as shown in Table 2. Many of the reported ALD NiO processes have not been thoroughly explored, with reports of temperature windows, precursor saturation studies, and growth-per-cycle (GPC) measurements significantly lacking. Reported growth temperatures are in the range of 100−275 °C, which is relatively low for TMO ALD processes.[24] Despite promising material properties, the NiO ALD processes in Table 2 typically suffer from low growth rates, with GPC values typically ranging from 0.01 to 0.08 nm/cycle. The highest reports are 0.13−0.14 nm/cycle for a Ni(dmamb)$_2$ and H_2O process[25] and, very recently, 0.2 nm/cycle for a Ni(acac)$_2$(TMEDA) and O_3 process.[26] However, both appear to exhibit fairly slow reaction kinetics.

Received: May 22, 2019
Accepted: July 25, 2019
Published: July 25, 2019

DOI: 10.1021/acsami.9b08926
ACS Appl. Mater. Interfaces 2019, 11, 30437−30445

Very recently, ALD growth of metallic Ni has been demonstrated using a newly developed diazadienyl precursor complex, bis(1,4-di-*tert*-butyl-1,3-diazadienyl)nickel [Ni($^{t\text{Bu2}}$DAD)$_2$] and *tert*-butylamine.[27] An analogous precursor, Co($^{t\text{Bu2}}$DAD)$_2$, has been used to achieve ALD of both metallic cobalt[28,29] using either formic acid, *tert*-butylamine, or diethylamine, and cobalt oxide[30] using ozone (O_3), as coreactants. In this work, we have taken a similar approach and developed a novel process for the ALD of NiO utilizing O_3 in combination with Ni($^{t\text{Bu2}}$DAD)$_2$. In this work, we thoroughly examine the ALD process space, including GPC versus deposition temperature, precursor and reactant saturation curves, film uniformity, and precursor temperature studies. The optical, structural, and elemental properties of as-deposited ALD NiO films were investigated using variable angle spectroscopic ellipsometry (VASE), grazing-incidence X-ray diffraction (GIXRD), atomic force microscopy (AFM), and X-ray photoelectron spectroscopy (XPS). Additionally, a heterojunction p-NiO/n-Si diode was fabricated to demonstrate the semiconducting nature of the ALD NiO thin films in device applications.

EXPERIMENTAL SECTION

ALD of NiO was carried out in a Picosun SUNALE R-150B reactor at ~1 Torr using alternating N_2-purge-separated pulses of Ni($^{t\text{Bu2}}$DAD)$_2$ and O_3/O_2. The temperature of the Ni($^{t\text{Bu2}}$DAD)$_2$ source was set between 100 and 160 °C and was delivered by a Picosun PicoSolid Booster source. O_3 was generated in an IN-USA AC-2025 ozone generator operated at 50% power, yielding an expected mixture of 10% O_3/O_2.

The optical, morphological, and growth properties of ALD films were measured on films deposited on ⟨111⟩ Si substrates with a 1.6 nm native SiO_x layer. Growth was also measured on Si substrates with 40 nm sputtered TiN and with 100 nm thermally grown SiO_2. Film thicknesses and refractive indices (including for the native SiO_x layer) were measured using a J.A. Woollam M2000 variable angle spectroscopic ellipsometer (VASE) in the wavelength range of 300−1000 nm. Film crystal properties were investigated via grazing-incidence X-ray diffraction (GIXRD) using a Rigaku Ultima IV diffractometer with Cu Kα radiation (λ = 1.5406 Å). Surface roughness was measured using an Asylum AFM system in air with Tap150Al-G cantilevers in the AC tapping mode. Elemental analysis was performed using X-ray photoelectron spectroscopy (XPS) on a Thermo K-Alpha+ with a 128 channel 180° hemispherical analyzer, a base pressure of 1×10^{-9} mbar and a monochromatic Al source with a spot size of 400 μm and a beam current of 6 mA. Measurements taken with the electron flood gun and sputtering was performed with 1 keV Ar ions. Data were analyzed using the Thermo Avantage V5.977 software package. For depth profiles, a "snapshot" mode (uses bands in the detector) was used with a pass energy of 149.613 eV; 5 frames at 1 s per frame. For other spectra, a scanned mode with 10 scans, a pass energy of 50 eV, a step size of 0.1 eV, and a dwell time of 50 ms was used.

Heterojunction pn diodes were fabricated by depositing ~50 nm of ALD NiO onto n-type ($N_D \approx 10^{18}$ cm^{-3}) or p-type ($N_A \approx 10^{19}$ cm^{-3}) ⟨111⟩ Si substrates with an ~1.6 nm native SiO_x layer. Circular Ag top electrodes with diameters of ~250 μm were thermally evaporated through a shadow mask onto the ALD NiO/n-Si substrate. The area of the top electrodes was measured with an optical microscope and used for calculating current density. Bottom electrodes were created by scratching through the ALD NiO layer with a diamond scribe and soldering indium contacts to the underlying n-Si substrate. Current−voltage measurements were taken in a dark box using a probe station and an Agilent B1500A semiconductor parameter analyzer. A Jandel RM2 four-point probe was used for measuring the resistivity of NiO films deposited on an insulating 100 nm thermal SiO_2/Si substrate. Five measurements were taken (center and four corners) on 1″ × 1″ square samples and thicknesses measured with VASE were used to calculate resistivity.

RESULTS

ALD Process Development. Shown in Figure 1 is a plot of NiO_x GPC versus deposition temperature (T_{dep}) on Si substrates with an ~1.6 nm layer of native SiO_x. ALD was carried out using a 5/30/4/30 s Ni($^{t\text{Bu2}}$DAD)$_2$/N_2/O_3/N_2 pulse sequence with the temperature of the Ni($^{t\text{Bu2}}$DAD)$_2$ source ampoule (T_{source}) held at 150 °C. GPC was calculated using a linear regression fit to film thicknesses resulting from 50, 150, and 300 cycle depositions at each temperature—a representative plot for a T_{dep} of 200 °C is included as an inset. A narrow window of nearly constant GPC vs temperature was observed between 185 and 200 °C. Inside this temperature window, the GPC is ~0.12 nm/cycle. As seen in the inset, no nucleation cycles were required to initiate growth. We also observed immediate NiO film growth on SiO_2 and TiN substrates.

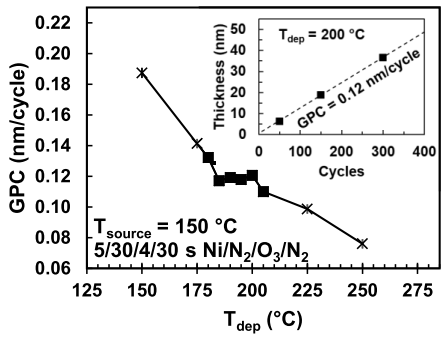

Figure 1. GPC versus temperature for alternating cycles of Ni($^{t\text{Bu2}}$DAD)$_2$ and O_3. Squares indicate the GPC calculated from the slope of film thicknesses vs cycles. Asterisks indicate GPC values calculated using only one thickness data point at 150 cycles. The inset plot shows NiO thickness versus a number of ALD cycles at T_{dep} = 200 °C; the dashed line represents a linear regression fit.

Shown in Figure 2 are saturation plots of GPC versus reactant pulse time for (a) Ni($^{t\text{Bu2}}$DAD)$_2$ and (b) O_3. GPC here was determined from either a 100- or 150-cycle deposition at each pulse time and error bars were calculated from the standard deviation of 50-point thickness maps taken across 1″ × 1″ samples. In Figure 2a, Ni($^{t\text{Bu2}}$DAD)$_2$ saturation was investigated for two Ni($^{t\text{Bu2}}$DAD)$_2$ source temperatures (T_{source} = 140 or 150 °C) and two deposition temperatures (T_{dep} = 190 and 200 °C) with the O_3 pulse time fixed at 4 s. At T_{dep} = 190 °C and T_{source} = 150 °C (black squares), saturation was reached after Ni($^{t\text{Bu2}}$DAD)$_2$ pulse times of about 2 s. For T_{dep} = 200 °C and T_{source} = 140 °C (green triangles) and T_{dep} = 200 °C and T_{source} = 150 °C (red circles), the Ni($^{t\text{Bu2}}$DAD)$_2$ saturation appears to be approached more gradually. For all three cases, the GPC at a Ni($^{t\text{Bu2}}$DAD)$_2$ pulse time of 10 s was equal within experimental error. Finally, a control run was conducted in which the O_3 pulses were omitted from a 150-cycle deposition carried out at 200 °C with 5 s Ni($^{t\text{Bu2}}$DAD)$_2$ pulses. No film growth occurred, ruling out any potential contributions from Ni($^{t\text{Bu2}}$DAD)$_2$ thermal decomposition.

In Figure 2b, with T_{dep} = 200 °C, T_{source} = 140 °C, and Ni($^{t\text{Bu2}}$DAD)$_2$ pulses fixed at 5 s, growth saturates for O_3 pulse times of around 4 s, typical for our O_3 delivery system,[31,32] and similar as for the Co($^{t\text{Bu2}}$DAD)$_2$ + O_3 process.[30]

DOI: 10.1021/acsami.9b08926
ACS Appl. Mater. Interfaces 2019, 11, 30437−30445

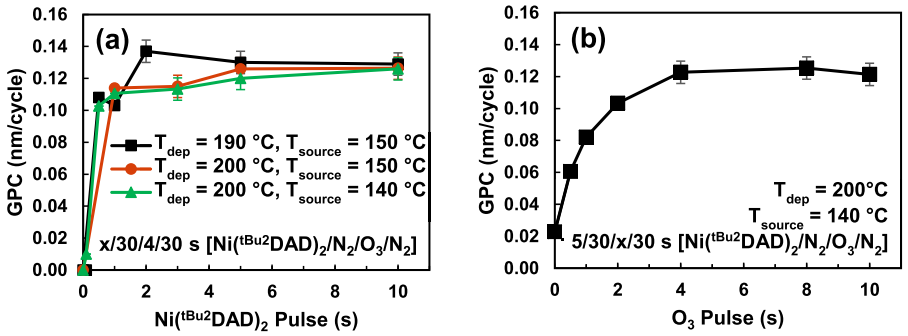

Figure 2. ALD saturation curves showing NiO GPC versus (a) Ni(^{tBu2}DAD)$_2$ and (b) O_3 pulse times using the indicated process conditions.

Shown in Figure 3 is a plot of GPC and nonuniformity versus Ni(^{tBu2}DAD)$_2$ T_{source} for 150-cycle depositions with T_{dep} fixed at 200 °C. GPC was measured on a 5″ wafer at a position near the Ni(^{tBu2}DAD)$_2$ inlet. Nonuniformity was calculated as the standard deviation/average thickness either (i) across the entire 5″ wafer (orange triangles) or (ii) within a 2.5″ diameter high uniformity zone (green diamonds, see dashed circles in Figure 4). At T_{source} = 100 °C, little growth occurred due to the lack of thermal energy required for volatilization. Growth increases substantially at 130 °C, reaching saturation at 140–160 °C, but the nonuniformity was only improved when T_{source} was increased to 150 °C and above, consistent with the data presented in Figure 2a. T_{source} = 150 °C was thus used in this work unless otherwise specified.

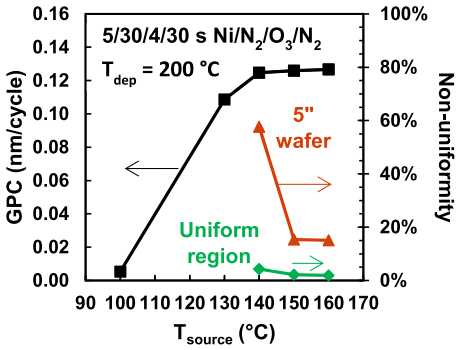

Figure 3. NiO GPC (squares) and percent nonuniformity calculated from either the full 5″ Si wafer area (triangles) or the 2.5″ diameter high uniformity region (diamonds, see Figure 4) versus T_{source}. Dosing conditions and ALD temperature are indicated.

To look at thickness nonuniformity more closely, thickness maps for these wafers are shown in Figure 4. For T_{source} = 140 °C, a uniform region is concentrated near the Ni(^{tBu2}DAD)$_2$ inlet with a steep drop-off in thickness outside the region, due to an insufficient Ni(^{tBu2}DAD)$_2$ dose. At T_{source} = 150 and 160 °C, film growth is spread more uniformly across the entire wafer, but still with the best uniformity near the Ni(^{tBu2}DAD)$_2$ inlet. Although nonuniformity below ~15% across the entire 5″ wafer is not obtained, extensive optimization of precursor delivery conditions in the R-150 deposition chamber (such as N_2 carrier gas flow balancing between the various precursor inlets, in this case too high for the O_3 inlet) was not performed. A systematic engineering optimization of chamber gas flow conditions would likely result in greatly increased uniformity over a larger surface area. Indeed, 2.5″ diameter circular regions (see dashed circles with different scale beneath full wafer) that exclude regions exhibiting the highest nonuniformity due to suboptimal conditions, show much improved uniformity over a fairly large area. The wafers at 150 and 160 °C show nonuniformity within the dashed circles of around 2%, consistent with a well-behaved ALD process. A plot of percent nonuniformity within the 2.5″ diameter high uniformity zones is shown in Figure 3 (green diamonds).

Additional Growth Studies. Growth of NiO using Ni(^{tBu2}DAD)$_2$ was also attempted using O_2 and H_2O as alternate oxidizing agents. For 500-cycle depositions with T_{dep} = 200 or 220 °C and T_{source} = 150 °C, no film growth was observed for 4 and 1 s pulses of O_2 and H_2O, respectively.

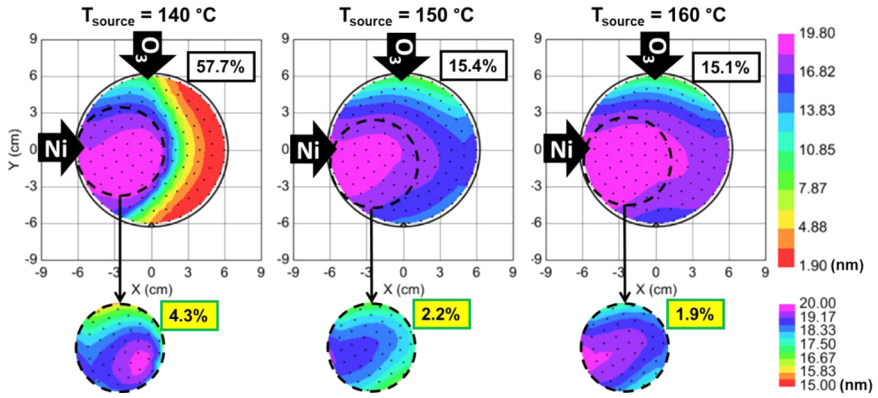

Figure 4. NiO thickness maps for 150-cycle runs at T_{dep} = 200 °C with different T_{source}. The position and flow direction of precursor inlets are indicated. 2.5″ regions excluding nonuniform areas are included below the full 5″ wafer maps with the corresponding scale bar. Percent nonuniformities across the full-wafers and within the dashed circles are indicated on the upper-right of the wafers.

DOI: 10.1021/acsami.9b08926
ACS Appl. Mater. Interfaces 2019, 11, 30437–30445

However, when T_{dep} was increased to 230 °C, a highly reflective, opaque, and conductive film (~75 μΩ cm and ~25 nm thick) was obtained, using either O_2 or H_2O. Removing the oxidizing agent from the pulse sequence (only Ni(^{tBu2}DAD)$_2$ pulses with otherwise the same deposition conditions) resulted in the same metallic film (~70 μΩ cm and ~20 nm thick), indicating the thermal decomposition of Ni(^{tBu2}DAD)$_2$ into metallic Ni. The average GPC of the Ni film deposited at 230 °C without any oxidizing agent is approximately 0.4 nm/cycle. When O_3 is included, the GPC of NiO at 230 °C is roughly double at 1.0 nm/cycle. Knisley et al.[33] found the thermal decomposition of Ni(^{tBu2}DAD)$_2$ to occur at 230 °C in the solid state and also reported the deposition of metallic Ni at this temperature.

Elemental Characterization. NiO samples deposited using 300 ALD cycles at T_{dep} = 150, 200, and 250 °C were measured using XPS to determine the elemental concentrations below, inside, and above the temperature window, respectively. A 60 s Ar sputter etch surface cleaning was performed prior to elemental analysis to remove any adventitious carbon acquired during shipment to the XPS facility. Shown in Table 1 are relative elemental concentrations

Table 1. Atomic Concentrations Determined with ±0.1% Accuracy via X-ray Photoelectron Spectroscopy (XPS) Following a 60 s Ar Sputter Surface Cleaning for Films Deposited at Various Temperatures

T_{dep} (°C)	Ni (%)	O (%)	C (%)	N (%)
150	52.4	46.4	1.2	0.7
200	53.7	46.3	<0.1	<0.1
250	53.9	46.1	<0.1	<0.1

of Ni, O, C, and N. At T_{dep} = 200 °C, no C or N was detected, likely due to sufficient thermal energy for O_3 to oxidize the organic ligands and thus any detectable trace of residual carbon. At 150 °C, below the ALD temperature window, only small amounts of C (1.2%) and N (0.7%) were detected. At 250, 20 °C above the thermal decomposition temperature of Ni(^{tBu2}DAD$_2$),[33] no C or N was detected. At all deposition temperatures, a Ni/O ratio in the range of 1.1:1 to 1.2:1 was observed. The slight O-deficiency can be explained by preferential sputtering of O during the pre-XPS 60 s Ar sputter surface cleaning.[34] Thus, the as-deposited films are expected to have Ni/O ratios much closer to unity than reported in Table 1. Depth profiling (Figure S1) showed constant composition throughout the film. Elemental XPS scans of the Ni 2p, O 1s, C 1s, and N 1s peaks for films deposited at 150, 200, and 250 °C following a 60 s Ar sputter cleaning are shown in Figure S2. The observed binding energy profiles are in good agreement with survey spectra for bulk NiO.[35]

Morphological Properties. A plot of GIXRD intensity vs 2θ is shown in Figure 5 for an ~18 nm thick ALD NiO sample deposited at 200 °C. Consistent with XPS, strong diffraction peaks corresponding to the cubic NiO crystal phase were detected, with no peaks attributable to the Ni_2O_3 phase. The relative intensities of the reference peaks for a randomly oriented cubic NiO powder specimen, indicated as solid vertical lines, match quite well to the data, indicating that as-deposited films have randomly oriented grains. Crystallite sizes of roughly ~8 nm with (111), (220), and (311) orientations

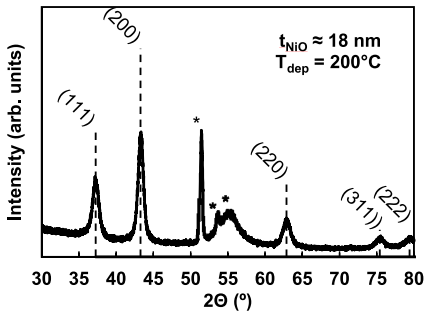

Figure 5. GIXRD spectrum for an ~18 nm thick NiO film deposited at 200 °C. Vertical lines indicate reference intensities for cubic NiO powder (PDF card #00-047-1049). Peaks matching a reference scan of the underlying Si substrate are indicated by asterisks (*).

and ~10 nm with (200) orientation were estimated using the Scherrer formula.

In Figure 6, an AFM image of the surface of an ~18 nm thick film deposited at 200 °C shows a root mean square

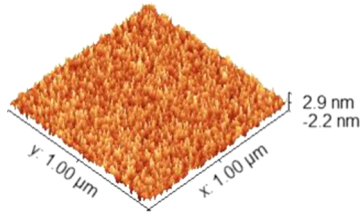

Figure 6. AFM 1 μm × 1 μm micrograph of an ~18 nm thick NiO film deposited at 200 °C.

(RMS) roughness of 0.6 nm (roughly 3% of the film thickness) and a maximum peak/valley height of 2.9/−2.2 nm.

Optical Properties. A study of the optical properties of a 32.5 nm thick NiO film grown at T_{dep} = 200 °C was conducted using VASE. Figure 7a shows a plot of the refractive index, RI, and extinction coefficient, k, versus incident wavelength, λ. An RI = 2.36 was obtained at λ = 632.6 nm. A strong absorption edge is seen in k versus λ for λ < 350 nm. To further examine the absorption behavior and provide an estimate for the bandgap, a Tauc plot was generated using the following relation[36]

$$(\alpha h\nu)^p \propto (h\nu - E_{opt}) \quad (1)$$

where α is the optical absorption at high frequency ($\alpha = 4\pi k/\lambda$, k is taken from Figure 7a), h is the Planck constant, ν is the incident light frequency, and p takes different values depending on the electronic transition (p = 2 or allowed direct transitions). In Figure 7b, extrapolation to the x-axis from the linear region of a Tauc plot of $(\alpha h\nu)^2$ versus incident photon energy, $h\nu$, shows an optical transition, E_{opt}, at approximately 3.78 eV, which is interpreted as the fundamental electronic bandgap, E_G. Inside the ALD window, the bandgap and RI are roughly constant between 3.7 and 3.8 eV and ~2.4, respectively (insets of Figure 7).

Electrical Characterization. In an attempt to measure resistivity, a four-point probe measurement was performed on a 49.7 nm NiO film deposited at 200 °C onto an insulating 100 nm thermally grown SiO_2/Si substrate. However, the exact resistivity of the film could not be determined above 50 Ω cm as the maximum voltage of the measurement system was exceeded.

DOI: 10.1021/acsami.9b08926
ACS Appl. Mater. Interfaces 2019, 11, 30437−30445

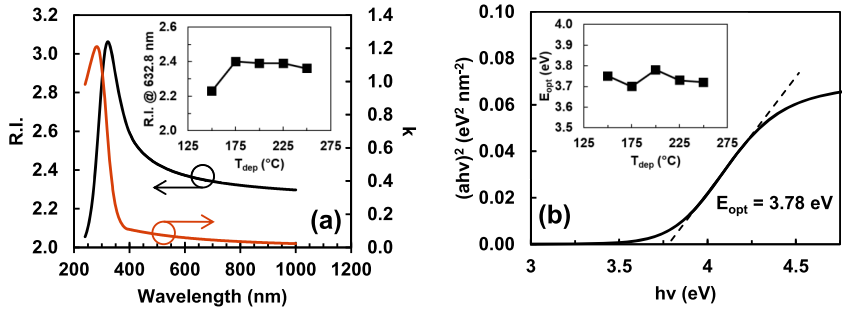

Figure 7. (a) RI and k versus λ and (b) Tauc plot of $(\alpha h\nu)^2$ vs $h\nu$ for a 32.5 nm thick NiO film deposited at 200 °C. Estimated E_{opt} is indicated. The inset figures show (a) RI at 632.8 nm incident wavelength and (b) E_{opt} versus T_{dep}.

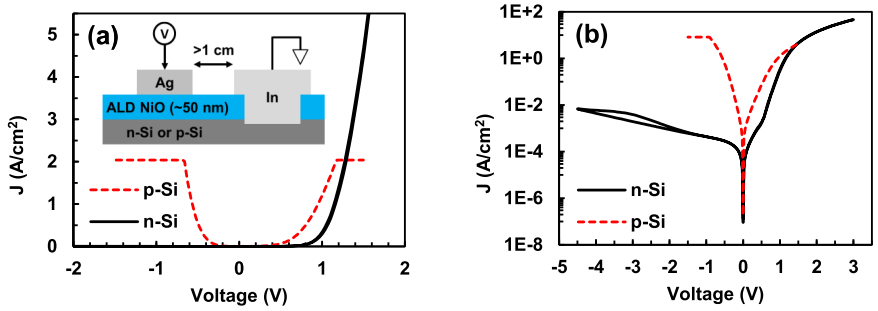

Figure 8. (a) Linear and (b) log-scale J–V sweeps of Ag/NiO/Si/In devices with either n-type (solid black lines) or p-type (dashed red lines) Si. The inset cross-sectional schematic in (a) depicts the device structure and biasing scheme.

Table 2. Summary of Reported ALD NiO Processes and Material Properties[a]

precursor	reactant	T_{dep} (°C)	GPC (nm/cycle)	nucleation cycles	ρ (Ω cm)	RI	E_{opt} (eV)	citation
Ni(^{tBu2}DAD)$_2$	O_3, O_2[b], H_2O[b]	185–200	0.12	0	>50	2.36	3.78	this work
Ni(acac)$_2$	O_3	250	0.06					39
Ni(acac)$_2$(TMEDA)	O_3	200–275[c]	0.2	0[d]				26
Ni(amd)$_2$	H_2O	175, 200	0.025–0.045, 0.075				3.55	40, 41
Ni(apo)$_2$	O_3	250						39
Ni(Cp)$_2$	O_3	150–275	~0.1, 0.063	100[d], 25[d]				42–47
	O_2	260						48
	O_2 plasma	225–275[c]	0.04-0.044	8			3.7	49
	H_2O	165						50
	O_3/H_2O	150	0.03					51
Ni(dmamb)$_2$	O_3	140–175,[c] 200	0.024, 0.034	0[d]		~2.35[d]	3.7–3.8	52, 53
	H_2O	130–150[c]	0.13-0.14	0[d]	10^7		3.52	25, 37, 38
Ni(dmamp)$_2$	H_2O	100–160[c]	0.08	0[d]				54
Ni(dmg)$_2$	O_3	250						39
Ni(EtCp)$_2$	O_3	200–300[c,d]	0.03, 0.05	0				44, 55
Ni(^{tBu2}amd)$_2$	H_2O	175	0.04					56
	H_2O	200	0.039			2.0–2.1	3.56	57
Ni(thd)$_2$	H_2O	230–260[d]	0.032–0.037	80[d]				58
	O_3	200	0.02		50		3.35–3.52	59

[a]Note that reported growth temperatures do not represent an ALD temperature window unless indicated. [b]Film growth did not occur using these reactants. [c]Indicates ALD temperature window. [d]Indicates our interpretation of the data.

To further assess electrical properties, heterojunction NiO/Si devices were fabricated using 52.7 nm ALD NiO films (deposited at T_{dep} = 200 °C) and either n-type Si or p-type Si substrates. Contacts to NiO and Si were made using Ag and In, respectively. Schematic cross-sections of the Ag/NiO/SiO_x (~1.6 nm)/Si/In devices are seen in the inset in Figure 8a. Note that due to the distance (>1 cm) between the In and Ag contacts, the measured high resistivity of NiO (>50 Ω cm), and the 52.7 nm thickness of the NiO, lateral leakage through the NiO film is not expected to make a significant contribution to the current density. Linear and log-linear current density (J) vs voltage (V) sweeps show strong asymmetry and nonlinearity for the n-type Si device, but roughly symmetric operation for the p-type Si device, indicating the p-type nature of the NiO. The p-NiO/n-Si heterojunction diodes reach a maximum J_+/J_- asymmetry of roughly 1.3 × 10^4 at 2.3 V.

DISCUSSION

ALD NiO Process. The approximately 185–200 °C ALD temperature window identified in this work for NiO deposited

DOI: 10.1021/acsami.9b08926
ACS Appl. Mater. Interfaces 2019, 11, 30437–30445

using Ni(^{tBu2}DAD)$_2$ and O_3 (Figure 1a) is very close to the 180−195 °C window reported by Kerrigan et al. for an ALD Ni metal process using Ni(^{tBu2}DAD)$_2$ with *tert*-butylamine as a coreactant.[27] The small 5 °C offset between the temperature windows could be explained by an offset error in the thermocouple reading of the ALD systems.

ALD processes with the diazadienyl complex Co(^{tBu2}DAD)$_2$, for metallic Co using either formic acid, *tert*-butylamine, or diethylamine, or Co_3O_4 using O_3, exhibit similarly narrow temperature window widths of ∼10 °C but at lower temperatures of 170−180 °C for formic acid, 170-200 °C for *tert*-butylamine, and 110−120 °C for O_3.[28−30] The similarity is likely related to the fact that these are analogous chemical structures, with both being four-coordinate diazadienyl complexes of metals in their 2+ oxidation states. Of the reported characteristics of the transition metal diazadienyl complexes synthesized by Knisley et al., the Ni and Co complexes are the most similar, with nearly equal thermal decomposition temperatures (Ni = 230 °C, Co = 235 °C), the same sublimation temperatures (115 °C at 0.05 Torr), and similar melting points (Ni ≈ 185 °C, Co ≈ 175 °C).[33]

The GPC in this work of 0.12 nm/cycle (Figures 1 and 2) for NiO is twice the reported value of Kerrigan et al.'s 0.06 nm/cycle for metallic Ni.[27] The increase in GPC is likely due to the replacement of the reducing half-cycle (*tert*-butylamine) with an oxidizing half-cycle (O_3) and the larger lattice constant of NiO vs Ni. The difference in GPC also appears to be present in the Co(^{tBu2}DAD)$_2$-based Co metal (∼0.1 nm/cycle)[28,29] and Co_3O_4 (0.11−0.12 nm/cycle)[30] ALD processes using either formic acid or O_3, respectively, albeit to a much smaller extent.

Table 2 contains a summary of previous reports of ALD NiO process details and associated material properties. Note that in many of these studies, the ALD process space is not fully explored (for example, ALD temperature windows, saturation curves, and plots of thickness versus the number of cycles are often missing). Generally, NiO ALD processes have suffered from low GPCs with very few reports of greater than 0.05 nm/cycle (see Table 2). We find that the GPC in the present work is among the highest of reported values for NiO, with reports of 0.13−0.14 nm/cycle for the Ni(dmamb)$_2$ + H_2O process[25,37,38] and 0.2 nm/cycle for the Ni(acac)2(TMEDA) + O_3 process.[26] However, both processes appear to exhibit a rather slow reaction kinetics with the Ni(dmamb)$_2$ + H_2O process space requiring long H_2O and Ni(dmamb)$_2$ pulses of >10 and >6 s, respectively, and the Ni(acac)$_2$(TMEDA) and O_3 process requiring a >4 s Ni(acac)$_2$(TMEDA) dose to reach saturating growth conditions.

At deposition temperatures below the NiO ALD window (<185 °C), GPC increases steeply (Figure 1) and it is likely that the reduced thermal energy allows physisorption or condensation of Ni(^{tBu2}DAD)$_2$ to dominate. Generally, condensation is accompanied by increased contamination from the residual elements contained in the precursor ligands and a deviation from the ideal stoichiometry. VASE shows the same E_{opt} at 150 °C as within the ALD window but a drop in RI from 2.4 to roughly 2.25. The XPS results for the film deposited at 150 °C (Table 1) show only slightly increased C (1.2%) and N (0.7%) contamination with the Ni/O ratio still quite close to unity. The low amount of impurities and near-unity Ni/O ratio, and similar optical properties are likely explained by the strong reactivity of O_3, which may be capable of reacting with most residual C or N impurities on the surface or subsurface to form volatile by-products and thereby form nearly stoichiometric NiO even at lower deposition temperatures. Note that Kerrigan et al. reported decreasing growth of metallic Ni with decreasing temperature using Ni(^{tBu2}DAD)$_2$ and *tert*-butylamine.[27] Although they did not suggest a mechanism for growth below the ALD window, the decreased growth they observe might be explained by a lack of available thermal energy to allow the reaction with *tert*-butylamine.

At deposition temperatures above the temperature window (205 °C), the NiO growth decreases sharply, followed by a continued gradual decrease with increasing temperature (Figure 1). This behavior is opposite to that reported by Kerrigan et al. for their *tert*-butylamine process. They saw increased growth of metallic Ni at 200 and 220 °C, which they attributed to the decomposition of Ni(^{tBu2}DAD)$_2$.[27] However, we find no direct evidence of thermal decomposition of Ni(^{tBu2}DAD)$_2$ in our system below 230 °C. Although Knisley et al. describe the thermal decomposition of Ni(^{tBu2}DAD)$_2$ to occur at 230 °C in the solid state, it is possible that the metal substrates used in the Kerrigan et al's work may have acted catalytically to lower the decomposition temperature of Ni(^{tBu2}DAD)$_2$ on the surface. At 230 °C and above, we observe CVD-like growth of a metallic Ni film when no oxidizing agent is used. Furthermore, XPS of a film deposited at 250 °C shows roughly the same 1.1:1 Ni/O stoichiometry (Table 1) and the RI and bandgap are nearly the same as films deposited within the ALD window , indicating that when metallic Ni is deposited via decomposition, it is subsequently oxidized in the presence of O_3. If thermal decomposition of Ni(^{tBu2}DAD)$_2$ is occurring above the ALD window, the observed reduction in GPC would mean that some of the decomposition would be occurring upstream of the wafer, leaving less precursor available for film growth on the wafer. In addition, XPS results (Table 1) show that film composition is not adversely affected, indicating that the ligand decomposition products must be effectively oxidized by O_3 into volatile by-products that are swept out of the chamber. Another possible cause of the decreased growth at temperatures above the ALD widow could be increasing desorption of Ni(^{tBu2}DAD)$_2$.

NiO Properties. GIXRD (Figure 5) indicates randomly oriented polycrystalline cubic NiO with an average grain size of ∼8 nm for an ∼18 nm thick film deposited at 200 °C. XPS elemental scans (Figure S1) match well with bulk NiO reference spectra and reveal that as-deposited films show no detectable impurity concentrations at 200 or 250 °C, both inside and above the temperature window, respectively (Table 1). E_{opt} and RI are also constant at these temperatures (inset of Figure 8).

AFM (Figure 6) shows an RMS roughness of roughly 0.6 nm for an approximately 18 nm thick film corresponding to a roughness/thickness ratio of ∼3%, slightly lower than the average of reported values in Table 2 of about ∼4.8%. Compared to ALD processes utilizing the same metalorganic precursor framework, the NiO roughness/thickness ratio of 3% is consistent with that reported for ALD Ni (∼3%)[27] using Ni(^{tBu2}DAD)$_2$ and *tert*-butylamine and ALD Co_3O_4 (∼3%)[30] using Co(^{tBu2}DAD)$_2$ and O_3, but slightly higher than that reported for the ALD Co process using Co(^{tBu2}DAD)$_2$ and formic acid (∼1%).[28]

The 200 °C as-deposited ALD NiO films in this work exhibit optical properties (RI = 2.36 and E_G = 3.78 eV) consistent with bulk NiO obtained from the flame-fusion method (RI = ∼2.36 to ∼2.45)[60,61] as well as thin film NiO

DOI: 10.1021/acsami.9b08926
ACS Appl. Mater. Interfaces 2019, 11, 30437−30445

obtained from ALD using Ni(dmamb)$_2$ + O_3 (RI = 2.35, E_G = 3.7−3.8 eV)[53] and Ni(dmamb)$_2$ + H_2O (E_G = 3.52 eV),[25] oxidation of Ni metal films at temperatures >400 °C (RI = 2.2−2.5, E_G = 3.35−3.85 eV),[62] and nebulized spray pyrolysis (RI = 2.1−2.4, E_G = 3.37−3.54).[20,21] The oxidized Ni films showed nearly identical optical properties likely due to the similar polycrystalline cubic structure with grain sizes of roughly 5−8 nm. The Ni(dmamb)$_2$ + O_3 ALD NiO films were also randomly oriented polycrystalline cubic with low levels of impurities determined by time-of-flight secondary ion mass spectrometry and thus also showed similar optical properties. Contrarily, the ALD NiO films deposited using Ni(dmamb)$_2$ and H_2O exhibited a lower bandgap.

p-NiO/n-Si Heterojunction Diode. As-deposited ALD NiO films are found to exhibit p-type semiconducting behavior. The $J-V$ response of heterojunction Ag/NiO/n-Si/In diodes (Figure 8) is highly rectifying, while the Ag/NiO/p-Si/In diodes are nearly symmetric. The maximum J_+/J_- asymmetry of 1.3 × 10^4 at 2.3 V for the Ag/NiO/n-Si/In diodes is in the range of maximum asymmetry values of 1.9 × 10^4 for an RF sputtered p-NiO/n-ZnO diode and ∼10^4 at 2.5 V for a sputtered p-NiO/n-IGZO diode.[2,4] In reverse bias, a soft saturation of the current is observed, as expected from a type I (straddling) heterojunction. A small amount of hysteresis is observed (with the increased current on the return sweep). As NiO is a relatively well-known resistive switching layer used for resistive random-access memory devices, the observed hysteresis may be due to a reduction in resistance caused by the formative stages of conductive nanofilaments;[18,19] however, this possibility was not studied further. Fitting the Shockley diode equation yields an ideality factor η = 3.5 which is outside the realm of a well-behaved pn-junction diode ($1 < \eta < 2$), but still in the range of reported values for NiO-based heterojunction diodes. Transparent p-NiO/n-ZnO and p-NiO/n-Ga_2O_3 diodes have been reported as having $\eta \approx 2-2.2$ and low $V_{ON} \approx 0.6-1.3$ V.[2,5−7] A p-NiO/n-IGZO diode was reported as having η = 4.3 and V_{ON} = 2.3 V.[4] A ALD p-NiO/n-TiO_2 diode deposited using Ni(amd) + H_2O exhibited $\eta \approx 4.1-4.5$.[40] p-NiO/n-Si diodes have been reported as having $\eta \approx 2.2$ and $V_{ON} \approx 2$ V for a Pt/sputtered p-NiO/n-Si/Al diode,[23] no clearly defined ideal region with $V_{ON} \approx 1$ V for a Pt/UV-oxidized p-NiO/n-Si/Au diode ($N_{D,Si} \approx 10^{15}$ cm^{-3}),[63] and η = 1.2 with V_{ON} = 0.8 V for a Ag/15 nm ALD p-NiO/n-Si diode ($N_{D,Si} = 10^{15}$ cm^{-3}), deposited using Ni(^{tBu2}amd)$_2$ + H_2O.[56] One potential explanation for the higher value of η in this work is the native SiO_x layer between the NiO and Si, which likely gives rise to interface states and increased carrier recombination and generation. The p-NiO/n-ZnO and p-NiO/n-Ga_2O_3 diodes, which exhibit lower η, were both deposited in vacuo[2,5−7] and thus likely contain sharper interfaces with fewer defects.

SUMMARY AND CONCLUSIONS

We demonstrate a new process for ALD of wide bandgap transparent p-type semiconducting NiO using Ni(^{tBu2}DAD)$_2$ and O_3. An ALD window was found between 185 and 200 °C with an optimal Ni(^{tBu2}DAD)$_2$ source temperature at 150 °C or above. Within the ALD window, a constant GPC of 0.12 nm/cycle was measured, among the highest GPC reported for NiO. GIXRD of films deposited at 200 °C indicates a randomly oriented polycrystalline cubic NiO consistent with XPS elemental analysis showing a Ni/O ratio near-unity, with <0.1% C or N impurities. VASE measurements indicate that the refractive index of 2.36 and extracted E_G of 3.8 eV are close to bulk values while AFM RMS roughness was 0.6 nm for an 18 nm thick film. Below the ALD window, condensation of Ni(^{tBu2}DAD)$_2$ results in uncontrolled growth with 1.2% C and 0.7% N impurities (XPS) at 150 °C. Above the window from 200 to 250 °C, films show low impurities (<0.1% C and N) but decreased GPC. Finally, fabricated Ag/NiO/n-Si/In heterojunction diodes show a current−voltage asymmetry of 1.3 × 10^4 at 2.3 V and an ideality factor of 3.5, while Ag/NiO/p-Si/In heterojunctions are found to be roughly symmetric, confirming the intrinsic p-type semiconducting behavior of as-deposited NiO.

Overall, the characterization performed in this work indicates that this new ALD NiO process using Ni(^{tBu2}DAD)$_2$ and O_3 shows promise for numerous transparent heterojunction device applications owing to its large bandgap and as-deposited p-type behavior. Additionally, the lower temperature ALD window opens the possibility for integration into the back end of the line of a CMOS process.

ASSOCIATED CONTENT

Supporting Information

The Supporting Information is available free of charge on the ACS Publications website at DOI: 10.1021/acsami.9b08926.

XPS sputter depth profile for a NiO film deposited at 200 °C using 300 cycles (Figure S1); XPS spectra of (a) Ni 2p, (b) O 1s, (c) C 1s, and (d) N 1s for NiO films deposited at the indicated ALD temperatures using 300 cycles (Figure S2) (PDF)

AUTHOR INFORMATION

Corresponding Author

*E-mail: jconley@eecs.oregonstate.edu.

ORCID

Konner E. K. Holden: 0000-0002-9806-0014

Present Address

§ASM Microchemistry Oy, Pietari Kalmin katu 3 F 2, 00560 Helsinki, Finland (C.L.D.).

Author Contributions

This manuscript was written through contributions of all authors. All authors have given approval to the final version of the manuscript.

Funding

National Science Foundation (grant ECC-1542101) Oregon State University, and RedWave Energy, Inc.

Notes

The authors declare no competing financial interest.

ACKNOWLEDGMENTS

The authors thank Chris Tasker for equipment support, Dr. Tom Polson and Dr. Dan Moser at EMD Performance Materials for XPS measurements and for providing Ni(^{tBu2}DAD)$_2$, respectively, and RedWave Energy Inc. for partial financial support. This work was conducted at the Materials Synthesis and Characterization (MaSC) Center, a National Nanotechnology Coordinated Infrastructure (NNCI) Northwest Nanotechnology Infrastructure (NWNI) user facility at the Oregon State University which is supported in part by the National Science Foundation (grant ECC-1542101) and Oregon State University.

DOI: 10.1021/acsami.9b08926
ACS Appl. Mater. Interfaces 2019, 11, 30437−30445

REFERENCES

(1) Tripathi, T. S.; Karppinen, M. Atomic Layer Deposition of p-Type Semiconducting Thin Films: A Review. *Adv. Mater. Interfaces* **2017**, *4*, No. 1700300.

(2) Hwang, J.; Lin, W. Enhancing the Photoresponse of p-NiO/n-ZnO Heterojunction Photodiodes Using Post ZnO Treatment. *IEEE Trans. Nanotechnol.* **2019**, *18*, 126−131.

(3) Kobayashi, K.; Yamaguchi, M.; Tomita, Y.; Maeda, Y. Fabrication and Characterization of In−Ga−Zn−O/NiO Structures. *Thin Solid Films* **2008**, *516*, 5903−5906.

(4) Münzenrieder, N.; Zysset, C.; Petti, L.; Kinkeldei, T.; Salvatore, G. A.; Tröster, G. Room Temperature Fabricated Flexible NiO/IGZO pn Diode under Mechanical Strain. *Solid-State Electron.* **2013**, *87*, 17−20.

(5) Ohta, H.; Hirano, M.; Nakahara, K.; Maruta, H.; Tanabe, T.; Kamiya, M.; Kamiya, T.; Hosono, H. Fabrication and Photoresponse of a pn-Heterojunction Diode Composed of Transparent Oxide Semiconductors, p-NiO and n-ZnO. *Appl. Phys. Lett.* **2003**, *83*, 1029−1031.

(6) Ohta, H.; Kamiya, M.; Kamiya, T.; Hirano, M.; Hosono, H. UV-Detector Based on pn-Heterojunction Diode Composed of Transparent Oxide Semiconductors, p-NiO/n-ZnO. *Thin Solid Films* **2003**, *445*, 317−321.

(7) Pintor-Monroy, M. I.; Barrera, D.; Murillo-Borjas, B. L.; Ochoa-Estrella, F. J.; Hsu, J. W. P.; Quevedo-Lopez, M. A. Tunable Electrical and Optical Properties of Nickel Oxide (NiO_x) Thin Films for Fully Transparent NiO_x−Ga_2O_3 p−n Junction Diodes. *ACS Appl. Mater. Interfaces* **2018**, *10*, 38159−38165.

(8) Park, J. H.; Seo, J.; Park, S.; Shin, S. S.; Kim, Y. C.; Jeon, N. J.; Shin, H.-W.; Ahn, T. K.; Noh, J. H.; Yoon, S. C.; Hwang, C. S.; Seok, S., II Efficient $CH_3NH_3PbI_3$ Perovskite Solar Cells Employing Nanostructured p-Type NiO Electrode Formed by a Pulsed Laser Deposition. *Adv. Mater.* **2015**, *27*, 4013−4019.

(9) Xu, X.; Liu, Z.; Zuo, Z.; Zhang, M.; Zhao, Z.; Shen, Y.; Zhou, H.; Chen, Q.; Yang, Y.; Wang, M. Hole Selective NiO Contact for Efficient Perovskite Solar Cells with Carbon Electrode. *Nano Lett.* **2015**, *15*, 2402−2408.

(10) Wang, K.-C.; Jeng, J.-Y.; Shen, P.-S.; Chang, Y.-C.; Diau, E. W.-G.; Tsai, C.-H.; Chao, T.-Y.; Hsu, H.-C.; Lin, P.-Y.; Chen, P.; Guo, T.-F.; Wen, T.-C. p-type Mesoscopic Nickel Oxide/Organometallic Perovskite Heterojunction Solar Cells. *Sci. Rep.* **2014**, *4*, No. 4756.

(11) Irwin, M. D.; Buchholz, D. B.; Hains, A. W.; Chang, R. P. H.; Marks, T. J. P-Type Semiconducting Nickel Oxide as an Efficiency-Enhancing Anode Interfacial Layer in Polymer Bulk-Heterojunction Solar Cells. *Proc. Natl. Acad. Sci. U.S.A.* **2008**, *105*, 2783−2787.

(12) Fumeaux, C.; Herrmann, W.; Kneubühl, F. K.; Rothuizen, H. Nanometer Thin-Film Ni−NiO−Ni Diodes for Detection and Mixing of 30 THz Radiation. *Infrared Phys. Technol.* **1998**, *39*, 123−183.

(13) Fumeaux, C.; Herrmann, W.; Kneubühl, F. K.; Rothuizen, H.; Lipphardt, B.; Weiss, C. O. Mixing of 28 THz (10.7 Mm) CO_2-Laser Radiation by Nanometer Thin-Film Ni-NiO-Ni Diodes with Difference Frequencies up to 176 GHz. *Infrared Phys. Technol.* **1997**, *38*, 393−396.

(14) Fumeaux, C.; Herrmann, W.; Kneubühl, F.; Rothuizen, H.; Lipphardt, B.; Weiss, C. O. Nanometer Thin-Film Ni-NiO-Ni Diodes for Mixing 28 THz CO_2-Laser Emissions with Difference Frequencies up to 176 GHz. *Appl. Phys. B: Lasers Opt.* **1998**, *66*, 327−332.

(15) Zhang, S.; Wang, L.; Xu, C.; Li, D.; Chen, L.; Yang, D. Fabrication of Ni-NiO-Cu Metal-Insulator-Metal Tunnel Diodes via Anodic Aluminum Oxide Templates. *ECS Solid State Lett.* **2012**, *2*, Q1−Q4.

(16) Singh, A.; Ratnadurai, R.; Kumar, R.; Krishnan, S.; Emirov, Y.; Bhansali, S. Fabrication and Current−Voltage Characteristics of NiO_x/ZnO Based MIIM Tunnel Diode. *Appl. Surf. Sci.* **2015**, *334*, 197−204.

(17) Singh, A.; Bhansali, S.; Barton, D.; Urban, F. K. Reactive Sputter Deposition and Annealing of Nanometer Scale NiO Thin Films for Metal-Insulator-Metal Tunnel Junction Diodes. *Thin Solid Films* **2017**, *644*, 23−28.

(18) Wong, H.-S. P.; Lee, H.-Y.; Yu, S.; Chen, Y.-S.; Wu, Y.; Chen, P.-S.; Lee, B.; Chen, F. T.; Tsai, M.-J. Metal-Oxide RRAM. *Proc. IEEE* **2012**, *100*, 1951−1970.

(19) Kinoshita, K.; Tamura, T.; Aoki, M.; Sugiyama, Y.; Tanaka, H. Lowering the Switching Current of Resistance Random Access Memory Using a Hetero Junction Structure Consisting of Transition Metal Oxides. *Jpn. J. Appl. Phys.* **2006**, *45*, L991−L994.

(20) Gowthami, V.; Meenakshi, M.; Perumal, P.; Sivakumar, R.; Sanjeeviraja, C. Optical Dispersion Characterization of NiO Thin Films Prepared by Nebulized Spray Technique. *Int. J. ChemTech Res.* **2014**, *6*, 5196−5202.

(21) Patil, P. S.; Kadam, L. D. Preparation and Characterization of Spray Pyrolyzed Nickel Oxide (NiO) Thin Films. *Appl. Surf. Sci.* **2002**, *199*, 211−221.

(22) Kang, J.-K.; Rhee, S.-W. Chemical Vapor Deposition of Nickel Oxide Films from $Ni(C_5H_5)_2/O_2$. *Thin Solid Films* **2001**, *391*, 57−61.

(23) Zhang, L.; Xu, H.; Wang, Z.; Liu, W.; Shi, K.; Lin, Y.; Liu, Y. p-NiO/n^+-Si Single Heterostructure for One Diode-One Resistor Memory Applications. *J. Alloys Compd.* **2017**, *721*, 520−524.

(24) Miikkulainen, V.; Leskelä, M.; Ritala, M.; Puurunen, R. L. Crystallinity of Inorganic Films Grown by Atomic Layer Deposition: Overview and General Trends. *J. Appl. Phys.* **2013**, *113*, No. 021301.

(25) Ko, M.-H.; Shong, B.; Hwang, J.-H. Low Temperature Atomic Layer Deposition of Nickel Sulfide and Nickel Oxide Thin Films Using $Ni(dmamb)_2$ as Ni Precursor. *Ceram. Int.* **2018**, *44*, 16342−16351.

(26) Zhang, Y.; Du, L.; Liu, X.; Ding, Y. A High Growth Rate Atomic Layer Deposition Process for Nickel Oxide Film Preparation Using a Combination of Nickel(II) Diketonate−Diamine and Ozone. *Appl. Surf. Sci.* **2019**, *481*, 138−143.

(27) Kerrigan, M. M.; Klesko, J. P.; Blakeney, K. J.; Winter, C. H. Low Temperature, Selective Atomic Layer Deposition of Nickel Metal Thin Films. *ACS Appl. Mater. Interfaces* **2018**, *10*, 14200−14208.

(28) Klesko, J. P.; Kerrigan, M. M.; Winter, C. H. Low Temperature Thermal Atomic Layer Deposition of Cobalt Metal Films. *Chem. Mater.* **2016**, *28*, 700−703.

(29) Kerrigan, M. M.; Klesko, J. P.; Winter, C. H. Low Temperature, Selective Atomic Layer Deposition of Cobalt Metal Films Using Bis(1,4-Di-Tert-Butyl-1,3-Diazadienyl)Cobalt and Alkylamine Precursors. *Chem. Mater.* **2017**, *29*, 7458−7466.

(30) Kim, J.; Iivonen, T.; Hämäläinen, J.; Kemell, M.; Meinander, K.; Mizohata, K.; Wang, L.; Räisänen, J.; Beranek, R.; Leskelä, M.; Devi, A. Low-Temperature Atomic Layer Deposition of Cobalt Oxide as an Effective Catalyst for Photoelectrochemical Water-Splitting Devices. *Chem. Mater.* **2017**, *29*, 5796−5805.

(31) Holden, K. E. K.; Conley, J. F., Jr. Characterization of Atomic Layer Deposited Semiconducting Co_3O_4. *J. Vac. Sci. Technol., A* **2019**, *37*, No. 020903.

(32) Holden, K. E. K.; Jenkins, M. A.; Conley, J. F., Jr. Characterization of Atomic Layer Deposited Cobalt Oxide. *ECS Trans.* **2018**, *85*, 735−741.

(33) Knisley, T. J.; Saly, M. J.; Heeg, M. J.; Roberts, J. L.; Winter, C. H. Volatility and High Thermal Stability in Mid- to Late-First-Row Transition-Metal Diazadienyl Complexes. *Organometallics* **2011**, *30*, 5010−5017.

(34) Mitchell, D. F.; Sproule, G. I.; Graham, M. J. Sputter Reduction of Oxides by Ion Bombardment during Auger Depth Profile Analysis. *Surf. Interface Anal.* **1990**, *15*, 487−497.

(35) Moulder, J. F.; Stickle, W. F.; Sobol, P. E.; Bomben, K. D. *Handbook of X-ray Photoelectron Spectroscopy: A Reference Book of Standard Spectra for Identification and Interpretation of XPS Data*; Physical Electronics Division, Perkin-Elmer Corporation, 1992.

(36) Tauc, J.; Grigorovici, R.; Vancu, A. Optical Properties and Electronic Structure of Amorphous Germanium. *Phys. Status Solidi B* **1966**, *15*, 627−637.

(37) So, B.-S.; You, Y.-H.; Kim, K.-H.; Hwang, J.; Cho, W.; Lee, S. S.; Chung, T.-M.; Lee, Y. K.; Kim, C. G.; An, K.-S.; Kim, Y.-C.; Lee, Y.-H.; Seo, W.-S. Crystallization of Amorphous Silicon Thin Films

DOI: 10.1021/acsami.9b08926
ACS Appl. Mater. Interfaces 2019, 11, 30437−30445

Using Self-Limiting ALD of Nickel Oxide. *Electrochem. Solid-State Lett.* **2007**, *10*, J61−J64.
(38) Lee, J.-Y.; Kim, J.-E.; Hwang, J.-H.; Ahn, J.-P.; Lee, B. K.; Kim, S.-H.; Chung, T.-M.; Lee, S. S.; Kim, C. G.; An, K.-S. Comparison of Nonvolatile Memory Effects in Ni-Based Layered and Dotted Nanostructures Prepared through Atomic Layer Deposition. *Electrochem. Solid-State Lett.* **2011**, *14*, J41−J44.
(39) Utriainen, M.; Kröger-Laukkanen, M.; Niinistö, L. Studies of NiO Thin Film Formation by Atomic Layer Epitaxy. *Mater. Sci. Eng., B* **1998**, *54*, 98−103.
(40) Thimsen, E.; Martinson, A. B. F.; Elam, J. W.; Pellin, M. J. Energy Levels, Electronic Properties, and Rectification in Ultrathin p-NiO Films Synthesized by Atomic Layer Deposition. *J. Phys. Chem. C* **2012**, *116*, 16830−16840.
(41) Nam, W. J.; Gray, Z.; Stayancho, J.; Plotnikov, V.; Kwon, D.; Waggoner, S.; Shenai-Khatkhate, D. V.; Pickering, M.; Okano, T.; Compaan, A.; Fonash, S. J. ALD NiO Thin Films As a Hole Transport-Electron Blocking Layer Material for Photo-Detector and Solar Cell Devices. *ECS Trans.* **2015**, *66*, 275−279.
(42) Nardi, K. L.; Yang, N.; Dickens, C. F.; Strickler, A. L.; Bent, S. F. Creating Highly Active Atomic Layer Deposited NiO Electrocatalysts for the Oxygen Evolution Reaction. *Adv. Energy Mater.* **2015**, *5*, No. 1500412.
(43) Alburquenque, D.; Del Canto, M.; Arenas, C.; Tejo, F.; Pereira, A.; Escrig, J. Dewetting of Ni Thin Films Obtained by Atomic Layer Deposition Due to the Thermal Reduction Process: Variation of the Thicknesses. *Thin Solid Films* **2017**, *638*, 114−118.
(44) Lu, H. L.; Scarel, G.; Wiemer, C.; Perego, M.; Spiga, S.; Fanciulli, M.; Pavia, G. Atomic Layer Deposition of NiO Films on Si (100) Using Cyclopentadienyl-Type Compounds and Ozone as Precursors. *J. Electrochem. Soc.* **2008**, *155*, H807−H811.
(45) Yu, L.; Wan, G.; Qin, Y.; Wang, G. Atomic Layer Deposition Assisted Fabrication of High-Purity Carbon Nanocoil for Electrochemical Energy Storage. *Electrochim. Acta* **2018**, *268*, 283−294.
(46) Yang, P.; Tong, X.; Wang, G.; Gao, Z.; Guo, X.; Qin, Y. NiO/SiC Nanocomposite Prepared by Atomic Layer Deposition Used as a Novel Electrocatalyst for Nonenzymatic Glucose Sensing. *ACS Appl. Mater. Interfaces* **2015**, *7*, 4772−4777.
(47) Zhang, R.; Wei, H.; Si, W.; Ou, G.; Zhao, C.; Song, M.; Zhang, C.; Wu, H. Enhanced Electrocatalytic Activity for Water Splitting on NiO/Ni/Carbon Fiber Paper. *Materials* **2016**, *10*, No. 15.
(48) Jeong, M.-G.; Kim, I. H.; Han, S. W.; Kim, D. H.; Kim, Y. D. Room Temperature CO Oxidation Catalyzed by NiO Particles on Mesoporous SiO_2 Prepared via Atomic Layer Deposition: Influence of Pre-Annealing Temperature on Catalytic Activity. *J. Mol. Catal. A: Chem.* **2016**, *414*, 87−93.
(49) Hufnagel, A. G.; Henß, A.-K.; Hoffmann, R.; Zeman, O. E. O.; Häringer, S.; Fattakhova-Rohlfing, D.; Bein, T. Electron-Blocking and Oxygen Evolution Catalyst Layers by Plasma-Enhanced Atomic Layer Deposition of Nickel Oxide. *Adv. Mater. Interfaces* **2018**, *5*, No. 1701531.
(50) Chae, J.; Park, H.-S.; Kang, S. Atomic Layer Deposition of Nickel by the Reduction of Preformed Nickel Oxide. *Electrochem. Solid-State Lett.* **2002**, *5*, C64−C66.
(51) Yu, L.; Wang, G.; Wan, G.; Wang, G.; Lin, S.; Li, X.; Wang, K.; Bai, Z.; Xiang, Y. Highly Effective Synthesis of NiO/CNT Nanohybrids by Atomic Layer Deposition for High-Rate and Long-Life Supercapacitors. *Dalton Trans.* **2016**, *45*, 13779−13786.
(52) Seo, S.; Jae Park, I.; Kim, M.; Lee, S.; Bae, C.; Suk Jung, H.; Park, N.-G.; Young Kim, J.; Shin, H. An Ultra-Thin, Un-Doped NiO Hole Transporting Layer of Highly Efficient (16.4%) Organic−Inorganic Hybrid Perovskite Solar Cells. *Nanoscale* **2016**, *8*, 11403−11412.
(53) Premkumar, P. A.; Toeller, M.; Adelmann, C.; Meersschaut, J.; Franquet, A.; Richard, O.; Tielens, H.; Brijs, B.; Moussa, A.; Conard, T.; Bender, H.; Schaekers, M.; Kittl, J. A.; Jurczak, M.; Van Elshocht, S. NiO Thin Films Synthesized by Atomic Layer Deposition Using Ni(dmamb)2 and Ozone as Precursors. *Chem. Vap. Deposition* **2012**, *18*, 61−69.
(54) Yang, T. S.; Cho, W.; Kim, M.; An, K.-S.; Chung, T.-M.; Kim, C. G.; Kim, Y. Atomic Layer Deposition of Nickel Oxide Films Using Ni(dmamp)2 and Water. *J. Vac. Sci. Technol., A* **2005**, *23*, 1238−1243.
(55) Barr, M. K. S.; Assaud, L.; Wu, Y.; Laffon, C.; Parent, P.; Bachmann, J.; Santinacci, L. Engineering a Three-Dimensional, Photoelectrochemically Active p-NiO/i-Sb_2S_3 Junction by Atomic Layer Deposition. *Electrochim. Acta* **2015**, *179*, 504−511.
(56) Berg, A. H.; Sahasrabudhe, G. S.; Kerner, R. A.; Rand, B. P.; Schwartz, J.; Sturm, J. C. In *Electron-Blocking NiO/Crystalline n-Si Heterojunction Formed by ALD at 175 °C*, In 2016 74th Annual Device Research Conference (DRC), 2016; pp 1−2.
(57) Hsu, C.-C.; Su, H.-W.; Hou, C.-H.; Shyue, J.-J.; Tsai, F.-Y. Atomic Layer Deposition of NiO Hole-Transporting Layers for Polymer Solar Cells. *Nanotechnology* **2015**, *26*, No. 385201.
(58) Lindahl, E.; Ottosson, M.; Carlsson, J.-O. Atomic Layer Deposition of NiO by the $Ni(thd)_2/H_2O$ Precursor Combination. *Chem. Vap. Deposition* **2009**, *15*, 186−191.
(59) Hagen, D. J.; Tripathi, T. S.; Terasaki, I.; Karppinen, M. Microstructure and Optical Properties of Ultra-Thin NiO Films Grown by Atomic Layer Deposition. *Semicond. Sci. Technol.* **2018**, *33*, No. 115015.
(60) Gielisse, P. J.; Plendl, J. N.; Mansur, L. C.; Marshall, R.; Mitra, S. S.; Mykolajewycz, R.; Smakula, A. Infrared Properties of NiO and CoO and Their Mixed Crystals. *J. Appl. Phys.* **1965**, *36*, 2446−2450.
(61) Powell, R. J.; Spicer, W. E. Optical Properties of NiO and CoO. *Phys. Rev. B* **1970**, *2*, 2182−2193.
(62) Venter, A.; Botha, J. R. Optical and Electrical Properties of NiO for Possible Dielectric Applications. *S. Afr. J. Sci.* **2011**, *107*, 1−6.
(63) Zhang, D.; Nozaki, S.; Uchida, K. NiO/Si Heterostructures Formed by UV Oxidation of Nickel Deposited on Si Substrates. *J. Vac. Sci. Technol., B: Nanotechnol. Microelectron.: Mater., Process., Meas., Phenom.* **2014**, *32*, No. 031202.

DOI: 10.1021/acsami.9b08926
ACS Appl. Mater. Interfaces 2019, 11, 30437−30445